Contents lists available at ScienceDirect

Ultramicroscopy

journal homepage: www.elsevier.com/locate/ultramic

A comparison of two high spatial resolution imaging techniques for determining carbide precipitate type and size in ferritic 9Cr-1Mo steel

C. Liu[a], P.J. Heard[a,*], O.D. Payton[a], L. Picco[b], P.E.J. Flewitt[a,c]

[a] Interface Analysis Centre, H.H. Wills Physics Laboratory, University of Bristol, Bristol, BS8 1TL, UK
[b] Department of Physics, Virginia Commonwealth University, Richmond, 23284 VA, USA
[c] School of Physics, HH Wills Physics Laboratory, University of Bristol, Bristol, BS8 1TL, UK

ARTICLE INFO

ABSTRACT

Two high spatial resolution imaging techniques, focused gallium ion beam imaging in conjunction with XeF_2 gas (FIB/XeF_2) and high-speed atomic force microscopy (HS-AFM), were used to analyse 9Cr-1Mo ferritic steel samples, which had been exposed for extended periods to hot CO_2 gas containing traces of CO, H_2, H_2O and CH_4. The carbide precipitates embedded in the metal matrix were observed and their morphology, size and spatial distribution were quantified using these two techniques. The lower resolution of the FIB/XeF_2 imaging technique suggested that small carbide precipitates (<50 nm) may be missed, while the existence of a limited flow layer introduced by sample preparation may influence the HS-AFM results. The gallium ion beam was used to remove a thin oxide layer of approximately 50 nm from sample surfaces prior to FIB/XeF_2 imaging, avoiding the influence of surface contamination. HS-AFM provided higher resolution ($\sim$5 nm) than FIB/XeF_2 imaging. A quantitative comparison of the experimental data confirmed the value of both FIB/XeF_2 and HS-AFM for imaging carbide precipitates, while clarifying their strengths and limitations.

1. Introduction

In many industries variants of 9Cr-1Mo steel are used in structural components required for high temperature service [1]. For example, ferritic and martensitic 9Cr-1Mo steels are used for components in advance gas-cooled nuclear reactors (AGR) operated by EDF Energy in the UK. Exposure to hot carbon dioxide gas leads to the formation of a duplex oxide and carbide precipitates in the matrix metal [2,3]. The precipitates may include M_3C, M_7C_3, M_6C and $M_{23}C_6$ etc. [4–7] where M represents Fe, Mo and Cr. Carbon is deposited in the oxide layer according to the following reaction [8]:

$$2CO \rightarrow CO_2 + C\downarrow \tag{1}$$

Free carbon produced by Eq. (1) (the Boudouard reaction) diffuses into the bulk metal leading to the formation of carbide precipitates. Previous workers have evaluated the carbide precipitates in steels, such as chromium-based carbides $M_{23}C_6$ and M_7C_3, as well as the Mo-based carbide precipitates M_2C and M_6C, using X-ray diffraction for crystal structure, and transmission electron microscopy in conjunction with energy-dispersive X-ray analysis for composition [9,10]. Recently, a range of other techniques have been adopted including focused ion beam (FIB) [11] and contact mode high-speed atomic force microscopy

(HS-AFM) to quantify carbide precipitate morphology, size and spatial distribution [12].

In this paper, we explore the morphology, size and the spatial distribution of carbide precipitates formed in a 9Cr-1Mo steel using two high spatial resolution methods, FIB in conjunction with XeF_2 gas, and HS-AFM.

2. Materials and techniques

Experimental ferritic 9Cr-1Mo steel finned tube samples supplied by EDF Energy Ltd. were exposed to simulated AGR coolant gas consisting primarily of CO_2 with additions of H_2O, H_2, CH_4 and CO at 40 bar for different temperatures and times. The chemical composition of the bulk 9Cr-1Mo steel prior to ageing is shown in Table 1. For the present work, two samples were selected: Sample A exposed for 2542 h at 580 °C and sample B exposed for 3883 h at 640 °C. Sample A possessed a duplex oxide of thickness 71 μm at the fin tip and 45 $\pm$ 2 μm at the fin side, with an outer layer of magnetite and an inner layer of iron-chromium spinel. Sample B had entered "breakaway oxidation" and possessed a laminated oxide of thickness 282 μm at the fin tip and 187 $\pm$ 6 μm at the fin side. A range of carbide precipitates were present in the ferrite matrix of both samples.

---

* Corresponding author.
  E-mail address: peter.heard@bristol.ac.uk (P.J. Heard).

Table 1
Chemical composition of experimental ferritic 9Cr-1Mo steel samples prior to ageing.

Elements	C	S	Si	Mn	P	Cr	Mo	Ni	Co	Cu	Fe
Concentration (wt.%)	0.093	0.008	0.67	0.47	0.011	9.2	1.04	0.21	0.02	0.16	Balance
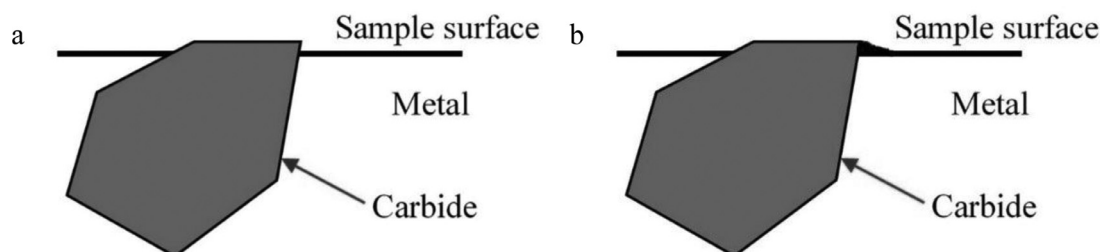
Fig. 1. Schematic diagram of a hard carbide precipitate at the sample surface prepared for HS-AFM analysis after polishing. (a) Idealised case and (b) with a limited flowed layer of softer metal trapped by the carbide edge.

The samples were mounted in cross-section and mechanically polished using a range of SiC abrasive papers and diamond pastes followed by vibro-polishing with a colloidal silica suspension to obtain finely polished surfaces suitable for optical microscopy and focused ion beam imaging.

Further sample surface preparation was required to ensure a high-quality surface for HS-AFM analysis. Samples selected for HS-AFM analysis were polished following the procedure presented by Warren et al. [13]. The topography of the resulting polished surface is expected to be determined by the relative hardness of the ferritic matrix and the carbide precipitates. The carbide precipitates would show a different height with respect to the metal surface due to their different hardness, making it possible to observe them using HS-AFM. Fig. 1 shows a schematic diagram of a carbide precipitate protruding from the matrix after polishing. Fig. 1a shows an idealised representation, but there is a potential for a limited flowed layer of metal to be present at the surface adjacent to a precipitate, as shown in Fig. 1b, that could be trapped by the edge of the carbide. This could distort the measurements made by modifying the apparent size of the carbide precipitate.

Two high-resolution techniques were employed to characterise the carbide precipitates present in the two samples.

Focused gallium ion beam induced secondary electron images were acquired using an FEI Helios NanoLab 600 dualbeam work station, operating at 30 keV gallium ion beam energy. FIB images were obtained initially by ion cleaning regions of the sample by sputtering an area of $51 \times 44\,\mu m$ at 21 nA beam current for about 10 s to remove surface contamination and oxide. Ion-induced secondary electron images were then obtained at 93 pA beam current showing topographical and ion channelling contrast. Following the acquisition of the initial images, XeF_2 gas was introduced into the system for about 2 s and further images were obtained. The resulting images had reduced ion channelling contrast but showed carbide precipitates as darker regions within a bright metal background. The mechanism for the accentuation of the carbide precipitates following the introduction of XeF_2 is not well established, but we propose a mechanism that is consistent with the following observations:

a) The XeF_2 only influences the image after the removal of surface contamination and oxide.
b) When XeF_2 is introduced into the chamber, the resulting pressure rise is approximately 10^{-5} mbar. This has a rapid effect on the image, taking only a few seconds to act, suggesting that only a monolayer of gas is required to modify the image.
c) The effect can be reversed by sputtering with the focused ion beam, again requiring the removal of approximately one monolayer of material.

d) The effect of exposure to XeF_2 is to make the metal brighter, while the carbide precipitates remain the same, so that a contrast is observed between them.

Based on these observations, we propose that the XeF_2 gas functionalises the clean metal surface, changing the work function of the material and increasing the secondary electron emission coefficient, while the exposed carbide surface remains unchanged. Hence the matrix metal becomes brighter in the FIB image, leaving the carbide precipitates a darker shade of grey. A series of 1024 x 884 pixel images of $51 \times 44\,\mu m$ were obtained in this way, traversing across a fin on the tube sample (Fig. 2a) at a distance of 1 mm from the tip to determine the carbide area fraction across the fin. Factors that determine the spatial resolution of this technique are the diameter of the ion beam, the interaction of the beam with the sample and the pixel size at the magnification used. In this case a beam current of 93 pA was used for imaging, giving a beam diameter of approximately 30 nm (value taken from manufacturer specification) but the pixel size at the magnification used was 50 nm, therefore the spatial resolution under these conditions was limited to the latter value.

HS-AFM images were acquired at 10 frames per second using a Bristol Nano Dynamics Ltd system which is capable of imaging at up to 2 Megapixels per second. Carbide precipitates and other features were identified by their height difference following polishing and utilising the greater carbide hardness compared with the parent matrix [13,14].

To automate the identification of carbides, a series of image filters and particle detection algorithms were implemented using LabVIEW modules in Bristol Nano Dynamics Ltd's Nanomapper software [15] as follows. Firstly, each frame was flattened to remove sample slope using "mean line flattening". This algorithm calculates a linear line of best fit to each column and row and then subtracts these lines from all the columns and rows to remove all slope in x and y. Secondly, carbides were separated from the bulk using the LabVIEW binary thresholding module. The binary image was then passed through the 'IMAQ Particle Analysis Report' (Vision Development, LabVIEW, National Instruments, USA) which measures the area and shape of each carbide identified [16]. The area of the carbides present in each frame is summed and divided by the area covered by the frame to give the carbide area fraction.

A set of 1600 overlapping HS-AFM images were obtained and stitched together to provide a large area high-resolution image for comparison with the FIB images. A series of HS-AFM images $4.5 \times 4.5\,\mu m$ in size were acquired and carbide area fractions were obtained as a function of position on the sample. Twenty such images were obtained, and the carbide area fractions plotted as a function of distance from the oxide/metal interface traversing across a fin at a distance of 1 mm from
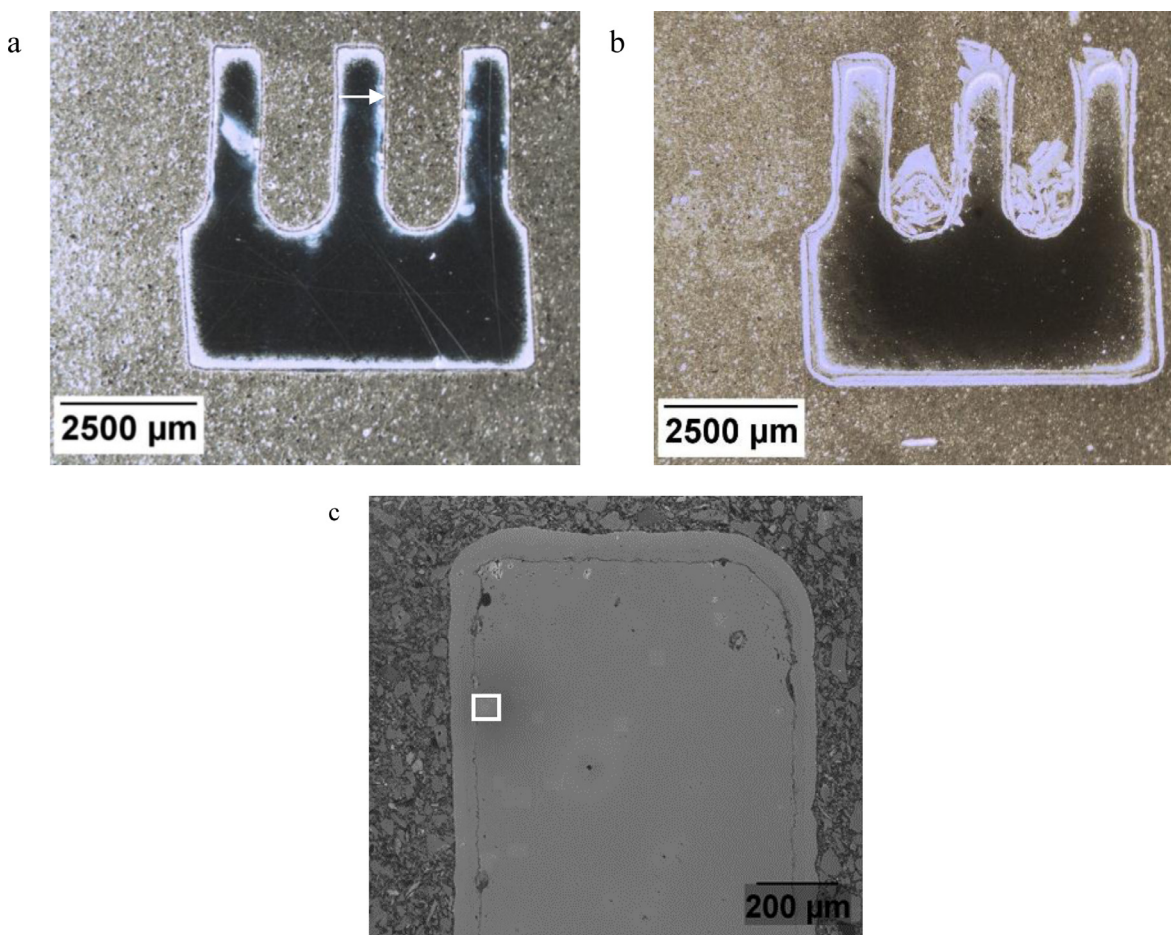
Fig. 2. Optical images of the samples set in resin (a) sample A with the path chosen for FIB imaging, (b) sample B and (c) FIB induced secondary electron image of the middle fin of sample A showing an area analysed using HS-AFM and FIB.

the fin tip. To characterise the carbide precipitate coverage further, a sparse matrix of images, each of $4.5 \times 1.5\,\mu m$ in size and spaced at 25 μm intervals were obtained, covering an extended 0.5 x 5 mm area of the fin. Carbide area fractions were extracted and colour-coded to provide a measure as a function of position. The spatial resolution of the technique is determined by the tip diameter, its interaction with the sample surface and the pixel size of the image. In this case, the tip radius approximately 2 nm, but the pixel size was 4.5 nm, so the image resolution was limited to the latter value.

3. Results

Optical images of the two prepared experimental finned tube samples A and B are shown in Figs. 2a and b. The central fin of sample A was analysed by FIB/XeF$_2$ and HS-AFM imaging following the path shown by the arrow in Fig. 2a. Fig. 2c shows a focused ion beam (FIB) induced secondary electron image of the central fin of sample A. An oxide layer of approximately 45 μm thickness is present at the fin side. The marked area shows a region near the oxide/metal interface that was analysed with both FIB/XeF$_2$ and HS-AFM imaging at high resolution for direct comparison.

Fig. 3 shows images of the region marked in Fig. 2c. A focused ion beam induced secondary electron image after surface cleaning is shown in Fig. 3a. The grains in the material are clearly visible due to the ion channelling contrast associated with FIB imaging. The corresponding image of the same area after exposure to XeF$_2$ gas is shown in Fig. 3b. The channelling contrast is now suppressed and the carbide precipitates are visible as darker regions in the image. It is evident that larger carbide precipitates are present at the grain boundaries, together with

smaller intragranular needle-shaped carbide precipitates. A section of the same image at higher magnification is shown in Fig. 3c. A HS-AFM image of the same region is shown in Fig. 3d. Clearly the FIB/XeF$_2$ image and the HS-AFM image are in general agreement regarding the morphology and distribution of carbide precipitates which are shown as dark areas in the FIB image and as brighter raised areas in the HS-AFM image. The coarse carbide precipitates at grain boundaries show a similar distribution in both the FIB/XeF$_2$ and HS-AFM images. The smaller needle-like intragranular carbide distribution is in general agreement between the two images, although there are small differences at higher magnification. For example, the region marked "1″" in Fig. 3c and d shows a needle-like carbide in the FIB/ XeF$_2$ image but not the HS-AFM image, while for the region marked "2″", the reverse is true. The reason for this is likely to be because the HS-AFM image was obtained before the FIB/XeF$_2$ image and the initial sputtering step to remove oxide and contamination prior to the FIB imaging will have removed a small amount of material that would explain this difference. An estimate of the ion-induced sputtering rate can be obtained from the Monte Carlo ion simulation program SRIM [17]. Using this, sputtering with a gallium ion beam at 21 nA current over a $51 \times 44\,\mu m$ area for 10 s would be expected to remove material to a depth of approximately 50 nm, which is comparable with the width of the small needle-shaped features. Such differences between the images are more prevalent when the long axis of the needle-like carbides is orientated parallel to the surface of the sample because it would be more likely that a small height change would either remove them or reveal buried ones. This is the case for grain A marked in Fig. 3d. When the needle-like carbides are orientated such that their long axis is normal to the surface of the sample, such differences are less likely, as for grain B. The HS-AFM
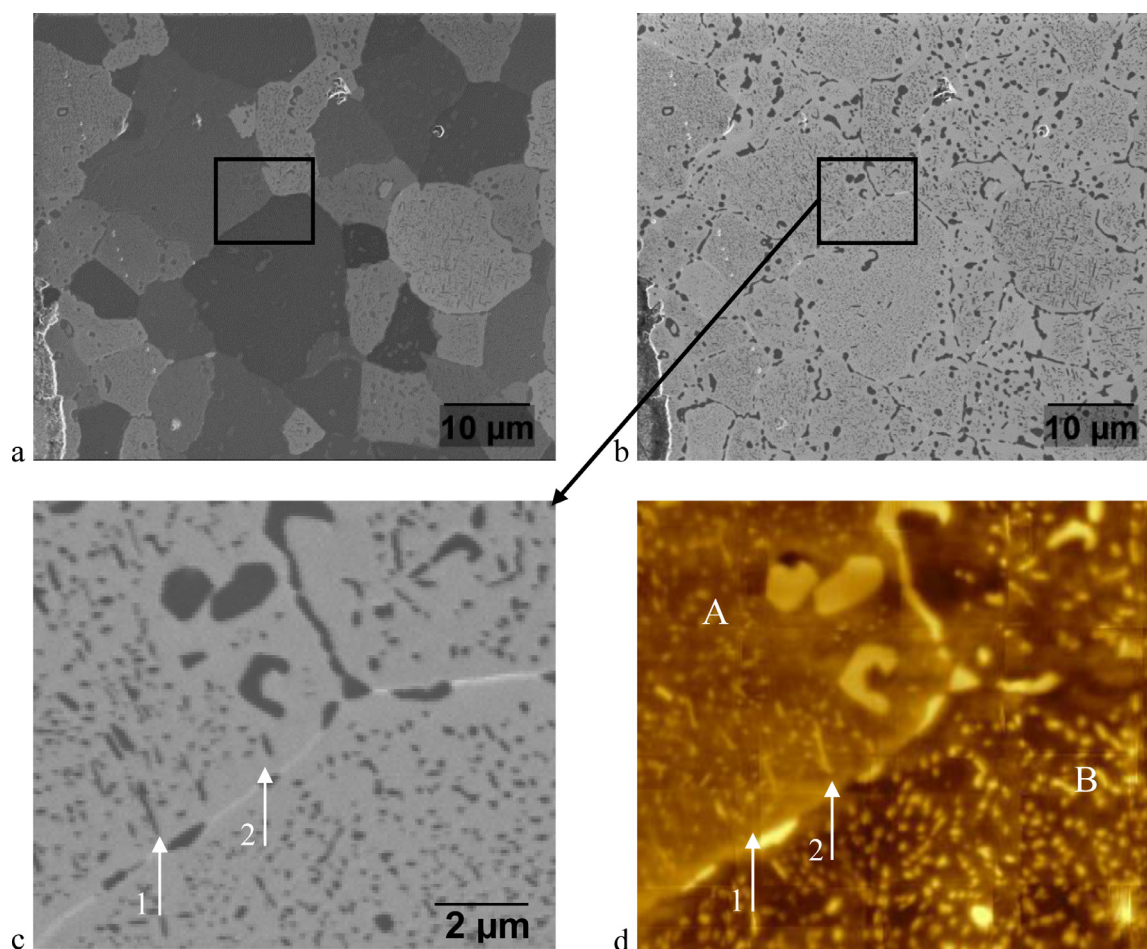
Fig. 3. (a) FIB induced secondary electron micrograph from sample A showing ion channelling contrast. (b) FIB induced secondary electron micrograph of the same area after introduction of XeF_2 gas. (c) Magnified region from image b. (d) Composite HS-AFM image from same area as c) (topographical height colour coded, 30 nm range). The FIB images were acquired after the HS-AFM images.

technique also reveals height changes from grain to grain, for example grain A and B marked in Fig. 3d differ in height by approximately 5–10 nm, with grain A being higher than grain B.

Fig. 4a and b show FIB/XeF_2 and the corresponding HS-AFM micrograph, respectively, from the middle fin of post-breakaway sample B. The HS-AFM image of Fig. 4b was constructed by stitching 1600 smaller images together to cover a larger area. Imperfections in the stitching process can be seen as a horizontal banding pattern in the image. A small area containing a coarse carbide precipitate is shown in Fig. 4c and d. From the contrast differences it is observed that many of the coarse carbide precipitates in this sample are "cored", possessing an inner region of a few micrometres diameter within an outer shell. The cores appear as a darker shade in the FIB/XeF_2 image, but brighter in the HS-AFM image revealing them to be higher than the surrounding shell which, in turn, is higher than the ferrite matrix. The carbide is of $M_{23}C_6$ type where M represents chromium or iron, and the core has been demonstrated to have a higher chromium content than the shell [18].

The HS-AFM images reveal that the core is harder than the shell, and there is a sharp interface between the two regions. The HS-AFM images also show further nanometre-scale height differences within the metal matrix that are remnants from the surface preparation with the colloidal silica.

Carbide precipitate area fractions for sample A were extracted from the FIB/XeF_2 and HS-AFM images and presented as a function of position on the fin to estimate the spatial extent of carburisation and to compare the capabilities of the two techniques. For the FIB/XeF_2 data,

16 images of size $51 \times 44\,\mu m$ at $55\,\mu m$ intervals were obtained across the width of the fin at a distance of 1 mm from the fin tip. The carbide area fractions were obtained using standard image processing software to threshold the images according to greyscale and count pixels corresponding to carbide precipitates. For the HS-AFM data, 18 images of $4.5 \times 1.5\,\mu m$ were captured at $25\,\mu m$ intervals to cover the right-hand half of the fin, again at a distance of 1 mm from the fin tip.

The total carbide area fractions for sample A obtained from both FIB/XeF_2 and HS-AFM images are shown in Fig. 5. They have a similar trend, however, the maximum value of area fraction derived from FIB/XeF_2 imaging is approximately 0.12, which is about 0.01 greater than the maximum value of 0.11 obtained from HS-AFM. Both profiles show a decrease in area fraction in the region close to the oxide on the right side of the fin. The minimum value of area fraction at the fin centre is approximately 0.03 from FIB/XeF_2 imaging and about 0.04 from HS-AFM. This is consistent with the known carbide precipitate content for un-carburised samples. The discrepancy for the lower area fractions may be because the smallest carbide precipitate sizes are beyond the resolution limit of the FIB/XeF_2 technique (50 nm), and therefore not detected.

The distribution of coarse and fine needle carbide precipitates was also investigated for sample A from the FIB/XeF_2 images by separating the carbide precipitates by area. Fig. 6 shows the distribution of these two types of carbide precipitates across the fin. The plots suggest that the total carbide area fraction is dominated by the coarse carbide precipitates, which contribute about 0.08–0.09 on the fin sides and about 0.03 in the fin centre. The fine needles are mainly distributed at the fin
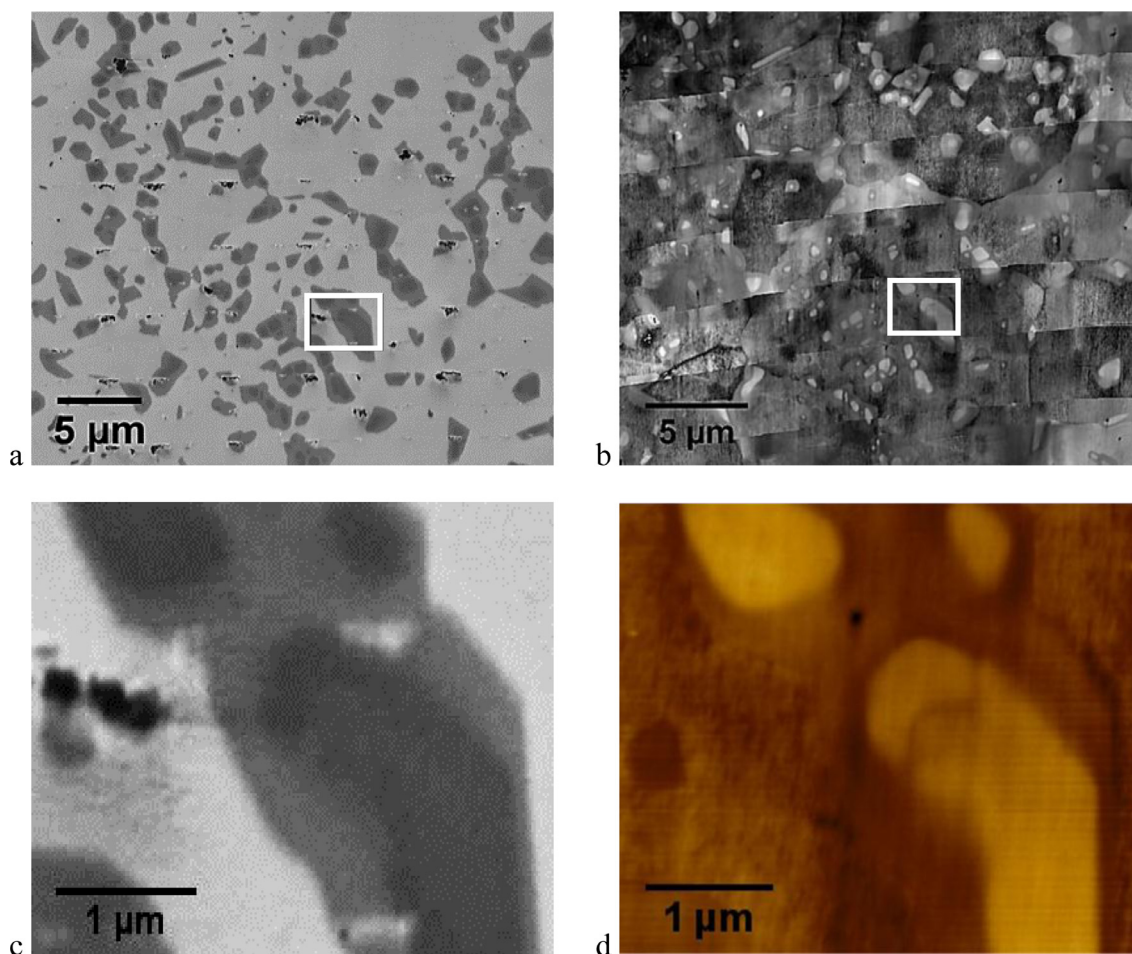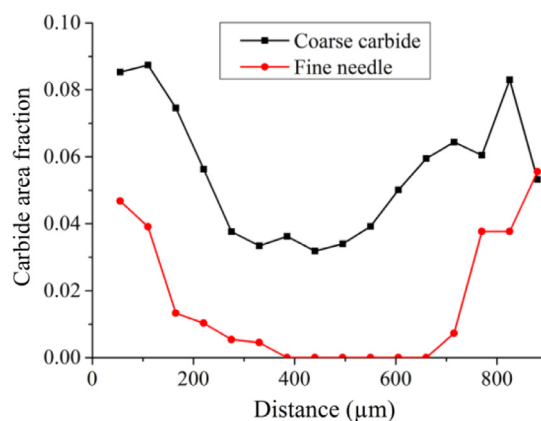
Fig. 4. (a) FIB induced secondary electron micrograph following XeF_2 exposure from sample B; (b) The composite HS-AFM image from same area showing horizontal banding due to imperfections in image stitching; (c) FIB/XeF_2 image at higher magnification (d) HS-AFM image of the same area as c) (topographical height colour coded, 15 nm range).
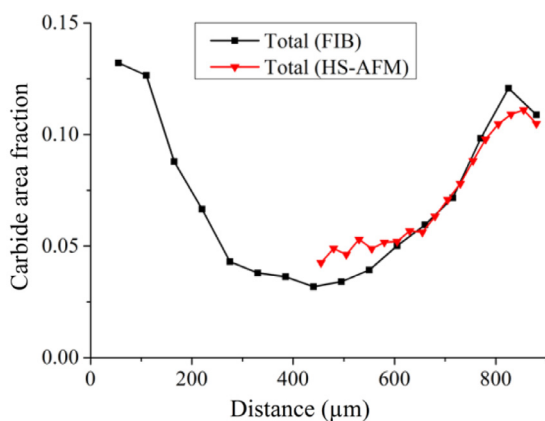
Fig. 5. The variation of carbide precipitate area fraction for sample A from both FIB/XeF_2 and HS-AFM images with distance from oxide/metal interface across the fin at 1 mm from the fin tip.

Fig. 6. The variation of carbide precipitate area fraction of coarse and needle carbides for sample A obtained from FIB/XeF_2 imaging with distance from oxide/metal interface across the fin at 1 mm from the fin tip. The coarse and fine precipitates were separated according to area.

sides, contributing about 0.04–0.06 area fraction and reducing to zero at the fin centre. The area fractions from both coarse and fine needle carbide precipitates decrease with increase of distance from the oxide/metal interface. The area fraction of fine needles reduces to zero in the fin centre at a distance of more than 400 μm from the oxide/metal interface. The minimum value of area fraction from coarse carbide precipitates is around 0.03 at 500 μm from the oxide/metal interface.

Carbide area fractions for sample A were extracted from HS-AFM images and colour coded to indicate the area fraction as a function of position. Fig. 7 shows the carbide percentages obtained overlaid with an optical image of the fin. To characterise the carbide coverage, a sparse matrix of images, each of $4.5 \times 1.5\,\mu m$ in size and spaced at 25 μm intervals were obtained, covering the entire right-hand side of the fin. It was observed that the carbide precipitates were mainly
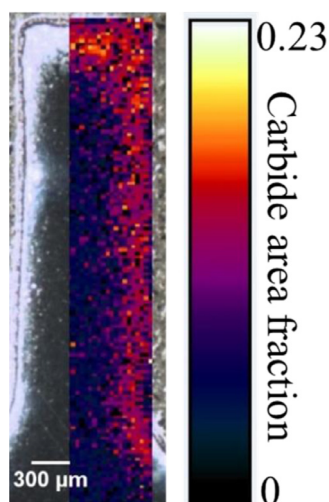
Fig. 7. Optical image of fin from sample A overlaid with a 0.5 × 5 mm HS-AFM map of carbide precipitate area fraction.

distributed beneath the oxide scale. This carbide precipitate area fraction map of the right-hand side of the middle fin obtained from sparse HS-AFM images shows that most carbide precipitates were distributed in the region about 200 μm from the fin side and 570 μm from the fin tip. Furthermore, the area fraction decreased with increase of distance from the oxide/metal interface and reached a minimum percentage at the fin centre.

4. Concluding comments

Two high spatial resolution techniques FIB/XeF$_2$ and HS-AFM have been used to image and quantify the carbide precipitates in two experimental samples of 9Cr-1Mo steel that had been exposed to CO$_2$ gas at high temperature for various times. Indeed, both techniques provide high quality images that enable the carbide precipitates to be observed to allow the morphology distribution and sizes of the precipitates to be evaluated.

In the case of the FIB/XeF$_2$ technique, the image is improved by removing a thin layer of oxide which is around 50 nm in thickness, to provide a clean surface and a change in work function by the adherence of XeF$_2$ gas to the sample surface [19–21]. Michaelson [20] has detailed the work function for many elements and provides values for Fe, Cr, and Mo as 4.5, 4.5 and 4.6 eV, respectively. Fujii et al. [22] investigated the work function values of a few types of MC and Cr$_3$C$_2$ carbide precipitates, which range from 4.8 to 5.2 eV. In general, more energy is required to release electrons from the carbide precipitates than the metal matrix. These data are consistent with FIB/XeF$_2$ imaging revealing carbide precipitates by raising the secondary electron emission coefficient of the ferrite matrix and suppressing channelling contrast, thus increasing the contrast between the carbide precipitates and the matrix.

In the case of HS-AFM, the imaging is based on the height of different features after polishing. The hardness of carbide precipitates such as M$_{23}$C$_6$, M$_2$C and M$_7$C$_3$ lies between approximately 10.7 and 22.6 GPa [23] which exceeds that of the matrix (ferrite containing alloying elements) where the hardness is approximately 3.5 to 3.9 GPa [24]. The HS-AFM image from sample B (Fig. 4d) which includes cored carbide precipitates reveals that the height is greater at the core indicating a higher hardness of the inner core than the outer layer carbide. As discussed by Liu et al. [25], the Cr concentration of the inner core and the shell carbide are between 40 and 80, and 30 and 50 wt%, respectively, indicating that the higher Cr concentration increases hardness for the carbide precipitates. Thus HS-AFM imaging of cored carbides is based upon the relative hardness of these three features: inner core > outer

layer carbide > matrix.

Sources of error for the FIB/XeF$_2$ technique result mainly from the imaging resolution which is around 50 nm. The diameter of the incident gallium ion beam with a current of 93 pA is approximately 30 nm (taken from manufacturer's specification) but the pixel size chosen here was 50 nm; therefore carbide precipitates of size less than this will not be resolved. This explains the smaller carbide area fraction measured at the fin centre from FIB/XeF$_2$ than HS-AFM as shown in Fig. 5. In the case of the HS-AFM technique the sources of potential error arise mainly from the following three factors: (1) The presence of flowed layers introduced by the preparation technique. Fig. 1b shows how some metal may be retained after polishing leading to a small distortion of the carbide precipitate image. It would make no difference for FIB/XeF$_2$ images but for HS-AFM analysis it would introduce an over-estimation of carbide precipitate size measurement. (2) The threshold level chosen in the image processing software which is based on the relative height of ferrite grains and carbide precipitates. Fig. 3d shows that the height of the ferrite matrix differs from grain A to grain B. Since the orientations will differ from grain to grain leading to an orientation dependence for the height, when this is combined with height differences for the carbide precipitates, threshold selection becomes difficult. Indeed, a dynamic thresholding algorithm that varies the threshold level according to position in the image will be required. (3) As discussed in Section 2, the sampling area of HS-AFM (4.5 × 4.5 μm) is much smaller than that of FIB/XeF$_2$ (51 × 44 μm). This leads to a statistical variation for the carbide area fraction, as shown in Fig. 5.

The comparative experiments between FIB/XeF$_2$ and HS-AFM imaging and their operating methods illustrate that both techniques can be used for carbide precipitate analysis. HS-AFM shows greater detail due to the higher spatial resolution of ∼5 nm compared with ∼50 nm for the FIB/XeF$_2$ technique. However, because the detection method based on the height of the matrix and carbide precipitates, the accuracy of HS-AFM results can be influenced by the presence of flowed material on the surface arising from sample preparation. FIB/XeF$_2$ provides better contrast between the ferritic matrix and carbide precipitates but the lower resolution leads to the observed under-estimation of carbide area fraction, because precipitates with sizes less than 50 nm are not resolved.

References

[1] S. Ukai, M. Harada, H. Okada, M. Inoue, S. Nomura, S. Shikakura, T. Nishida, M. Fujiwara, K. Asabe, Tube manufacturing and mechanical properties of oxide dispersion strengthened ferritic steel, J. Nucl. Mater. 204 (1993) 74–80.

[2] J.W. Taylor, AGR boiler materials selection considerations, Gas-Cooled Reactors Today, Today, British Nuclear Energy Society, Bristol, 1982, p. 328.

[3] G.B. Gibbs, L.A. Popple, Oxidation of structural steels in CO$_2$ cooled reactors, Nucl. Energy 21 (1982) 51–55.

[4] T. Gheno, D. Monceau, J. Zhang, D.J. Young, Carburisation of Ferritic Fe–Cr alloys by low carbon activity gases, Corros. Sci 53 (2011) 2767–2777.

[5] H.O. Andrén, G. Cai, L.E. Svensson, Microstructure of heat resistant chromium steel weld metals, Appl. Surf. Sci 87–88 (1995) 200–206.

[6] F. Rouillard, G. Moine, M. Tabarant, J.C. Ruiz, Corrosion of 9Cr Steel in CO$_2$ at intermediate temperature II: mechanism of carburization, Oxid. Met 77 (2012) 57–70.

[7] M. Vijayalakshmi, S. Saroja, V.T. Paul, R. Mythili, V.S. Raghunathan, Microstructural zones in the primary solidification structure of weldment of 9Cr-1Mo steel, Metall. Mater. Trans. A 30 (1999) 161–174.

[8] J. Hunt, A. Ferrari, A. Lita, M. Crosswhite, B. Ashley, A.E. Stiegman, Microwave-specific enhancement of the carbon–carbon dioxide (boudouard) reaction, J. Phys. Chem. C. 117 (2013) 26871–26880.

[9] A.I. Martinez-Ubeda, Effect of Composition Variation and Service Environment on the Long Term Ageing of Type 316H Austenitic Stainless Steels, PhD thesis University of Bristol, 2017.

[10] A.I. Martinez-Ubeda, A.D. Warren, I. Griffiths, P.E.J. Flewitt, The role of prior

fabrication and in service thermal ageing on the creep life of AISI Type 316 stainless steel components, Key Eng. Mater 713 (2016) 1–4.

[11] S.N. Bhavsar, S. Aravindan, P.V. Rao, Materials and manufacturing processes machinability study of cemented carbide using focused ion beam (FIB) milling, Mater. Manuf. Process 27 (2012) 1029–1034.

[12] A.I. Martinez-Ubeda, I. Griffiths, O.D. Payton, C.M. Younes, T.B. Scott, P.E.J. Flewitt, Role of long term ageing on the creep life of type 316H austenitic stainless steel bifurcation weldments, Mater. Fabr., ASME 6A (2016) p. V06AT06A058.

[13] A.D. Warren, A.I. Martinez-Ubeda, O.D. Payton, L. Picco, T.B. Scott, Preparation of stainless steel surfaces for scanning probe microscopy, Micros. Today 24 (2016) 52–55.

[14] O.D. Payton, L. Picco, T.B. Scott, High-speed atomic force microscopy for materials science, Int. Mater. Rev 61 (2016) 473–494.

[15] http://nanodynamics.co.uk/technology/unparalleled-sample-statistics (accessed June 2019) (2019).

[16] http://zone.ni.com/reference/en-XX/help/370281AE-01/imaqvision/imaq_particle_analysis_report/ (accessed June 2019) (2019).

[17] J.P. Biersack, L. Haggmark, A Monte-Carlo computer-program for the transport of energetic ions in amorphous targets, Nucl. Instr. and Meth. 174 (1980) 257–269.

[18] C. Liu, Oxidation and Carburisation of 9Cr-1Mo Steel in Both Simulant and In-service AGR Coolant Gases, PhD thesis University of Bristol, 2018.

[19] R. Smoluchowski, Anisotropy of the electronic work function of metals, Phys. Rev 60 (1941) 661–674.

[20] H.B. Michaelson, The work function of the elements and its periodicity, J. Appl. Phys. 48 (1977) 4729–4733.

[21] V. Guillaumin, P. Schmutz, G.S. Frankel, Characterization of corrosion interfaces by the scanning Kelvin probe force microscopy technique, J. Electrochem. Soc. 148 (2001) B163.

[22] R. Fujii, M.Y. Liao, H. Tsuji, J. Ishikawa, Work function measurement of transition metal nitride and carbide thin films, Vacuum 80 (2006) 832–835.

[23] B. Venkatesh, K. Sriker, V.S.V. Prabhakar, Wear characteristics of hardfacing alloys: state-of-the-art, Procedia Mater. Sci 10 (2015) 527–532.

[24] J. Moon, S. Kim, J. Jang, J. Lee, C. Lee, Orowan strengthening effect on the nanoindentation hardness of the ferrite matrix in microalloyed steels, Mater. Sci. Eng. A 487 (2008) 552–557.

[25] C. Liu, P.J. Heard, S.J. Greenwell, P.E.J. Flewitt, A study of breakaway oxidation of 9Cr-1Mo steel in a hot CO_2 atmosphere using Raman spectroscopy, Mater. High Temp 35 (2018) 50–55.